Single-cell spatial mapping reveals dynamic bone marrow microarchitectural alterations and enhances clinical diagnostics in MDS

Ryan Nachman,[1] Aleksandra Kopacz,[1] Caitlin Unkenholz,[1,4] Jian Chai, [2] Arvin Ruiz,[3] Itzel Valencia,[4] Jeanne Jiang,[4] Fabio Socciarelli,[4] Jiwoon Park,[5] Christopher Mason,[(5-8)] Ling Zhang,[9] David Sallman,[10] Gail J. Roboz,[11] Pinkal Desai,[11] Justin Kaner,[11] Joshua Fein,[11] Monica Guzman,[11] Neal Lindeman,[12] Amy Chadburn,[2] Madhu Ouseph,[2,12] Paul Simonson,[2] Julia Geyer,[2] Giorgio Inghirami,[2,3] Shahin Rafii,[1] David Redmond,[1*] Sanjay Patel[2,4*]

[1]Division of Regenerative Medicine, Hartman Institute for Therapeutic Organ Regeneration, Ansary Stem Cell Institute, Department of Medicine, Weill Cornell Medicine, New York, NY, USA

[2]Division of Hematopathology, Department of Pathology and Laboratory Medicine, Weill Cornell Medicine/NewYork-Presbyterian Hospital, New York, NY, USA [s]

[3]Immunopathology Laboratory, Weill Cornell Medical College/NewYork-Presbyterian Hospital, New York, NY, USA

[4]Multiparametric In Situ Imaging (MISI) Laboratory, Department of Pathology and Laboratory Medicine, Weill Cornell Medicine, New York, NY, USA

[5]Department of Physiology and Biophysics, Weill Cornell Medicine, New York, NY, USA

[6]The Feil Family Brain and Mind Research Institute, Weill Cornell Medicine, New York, NY

[7]WorldQuant Initiative for Quantitative Prediction, Weill Cornell Medicine, New York, NY

[8]The HRH Prince Alwaleed Bin Talal Bin Abdulaziz Alsaud Institute for Computational Biomedicine, Weill Cornell Medicine, New York, NY

[9]Department of Hematopathology and Laboratory Medicine, Moffitt Cancer Center, Tampa, FL, USA

[10]Department of Malignant Hematology, Moffitt Cancer Center, Tampa, FL, USA

[11]Division of Hematology and Medical Oncology, Department of Medicine, Weill Cornell Medicine/NewYork-Presbyterian Hospital, New York, USA

[12]Division of Molecular Genetic Pathology, Department of Pathology and Laboratory Medicine, Weill Cornell Medicine/NewYork-Presbyterian Hospital, New York

*Correspondence: Sanjay Patel, MD (sap9151@med.cornell.edu) & David Redmond, PhD (dar2042@med.cornell.edu) | Abstract word count: 186 | Main text word count (incl. Methods): ~4,300 | Main Table Count: 0 | Main Figure count: 6 | References: 48 | Supplemental Table count: 5 | Supplemental Figure count: 11

ABSTRACT

Myelodysplastic neoplasms (MDS) are genetically heterogeneous hematopoietic malignancies characterized by ineffective hematopoiesis, peripheral cytopenias, and risk of progression to acute myeloid leukemia. Diagnosis relies on subjective histomorphologic evaluation of bone marrow biopsies, leaving the significance of subtle microarchitectural changes unclear. We applied an AI-driven, whole-slide imaging–based multiplex immunofluorescence single-cell spatial phenotyping approach to diagnostic MDS samples (n=36), serial biopsies (n=29), precursor-state samples (n=13), and normal controls (n=21), profiling over 5 million cells. Compared with age-matched controls, MDS exhibited altered progenitor cell frequencies, abnormal erythroid and megakaryocyte morphology, disrupted erythroid islands, vascular displacement of hematopoietic stem and progenitor cells, and aberrant progenitor cell clustering. Several features correlated more strongly with specific mutations (e.g., *SF3B1*, *TP53*) than with IPSS-M risk scores. We integrated these features into a composite MDS Microarchitectural Perturbation Score (MDS-MAPS) that aligned with clinical and genetic parameters across serial samples, revealing previously unrecognized, genotype-associated microarchitectural alterations in MDS.

SIGNIFICANCE

AI-driven spatial mapping detects previously unrecognized microarchitectural perturbations in MDS patient bone marrow biopsy tissues. Microarchitectural perturbations track closely with clinical and genetic parameters during the course of disease-modifying therapy. The detection of these features holds the potential to additionally inform clinical evaluation alongside standard clinical parameters.

INTRODUCTION

Myelodysplastic neoplasms (MDS) develop as a result of clonal proliferation of hematopoietic stem cells and their progeny. They are defined by abnormal hematopoiesis, which manifests with peripheral cytopenias, their clinical sequelae, and a predisposition to acute leukemia.[1] A histopathologic evaluation is required to establish the diagnosis and involves subjective interrogation for cytologic features of dysplasia in hematopoietic cells, accompanied by overt architectural alterations in intact bone marrow trephine biopsy tissues, such as age-adjusted hypercellularity and abnormal megakaryocyte morphology.[2,3] The cornerstones for these assessments include tools that have not evolved considerably over the last few decades, such as light microscopy, single-marker immunohistochemistry, and flow cytometric immunophenotyping.[4] It is noteworthy that blast percentage, which is still derived through manual enumeration by trained practitioners, remains the only parameter incorporated into algorithms used for patient risk stratification.[5,6]

The rapidly evolving genomic era has greatly advanced our understanding of the cell-intrinsic genetic basis of MDS and led to improvements in the models currently used for patient risk stratification.[6] Nevertheless, optimal integration of morphologic, immunophenotypic, and genetic parameters remains highly controversial, as evidenced by recent struggles to harmonize the competing International Consensus Classification (ICC) and World Health Organization (WHO) MDS classification systems.[2,7] Importantly, these ancillary data are typically derived either from peripheral blood or aspirated bone marrow material, and therefore subject to artifacts of sampling; although this enables profiling of hundreds of thousands of cells, which can be easily repeated along the course of therapy, studies using liquid cell suspensions cannot provide information about the complex marrow microarchitecture. Despite these limitations, studies based on aspirated marrow have clearly indicated roles for cell-intrinsic *and* –extrinsic factors in MDS disease pathogenesis,[8] although reliable spatial architecture models of the disease that account for its clinical and genetic heterogeneity are still lacking.[9,10]

We recently developed an approach to perform in situ spatial mapping of human hematopoiesis using archival tissue samples, multiplex immunofluorescence tissue staining, whole slide imaging, and artificial

74 intelligence (AI)-based image analysis at single cell resolution;[11] our analysis of a cohort of normal bone marrow
75 samples revealed spatial patterns of hematopoiesis that were largely conserved with aging. Here, we have applied
76 this approach, and expanded upon our analytical methodology, to profile a cohort of clinically and genetically
77 annotated bone marrow tissue samples from MDS patients, including biopsies at multiple timepoints along the
78 course of standard-of-care therapy. Our findings reveal known, and also previously unrecognized, quantifiable
79 perturbations to the normal spatial microarchitecture of human hematopoiesis in MDS.
80

81 **RESULTS**

82 ***Characteristics of patient cohort***

83 We assembled a cohort of clinically and genetically annotated archival bone marrow trephine biopsy
84 samples collected as part of routine diagnostics at our academic medical center **(Figure 1a, Supplementary Data**
85 **Table 1)**. The cohort included 77 samples from 48 unique patients with either MDS (n=36) or the precursor state
86 clonal hematopoiesis of indeterminate potential/clonal cytopenia of unknown significance (CHIP/CCUS, n=13);
87 additionally, for 14 of the MDS patients, 29 serial samples collected along the course of pharmacologic
88 management, with or without eventual allogeneic hematopoietic stem cell transplantation (HSCT), were also
89 profiled. 21 normal bone marrow controls (NBMs), including age-matched samples, from a recently published
90 cohort were also analyzed.[11] Figures 1-6 include only diagnostic samples, while Figure 7 includes samples at
91 multiple timepoints, unless otherwise stated.

92 The median age among CHIP/CCUS and MDS patients was 77, with a M:F of 1:1. MDS samples were
93 categorized into those with low-blasts (MDS-LB, n=20) or with high-blasts (MDS-IB, n=16). International
94 Prognostic Scoring System-Molecular (IPSS-M) values were calculated for all diagnostic samples from MDS
95 patients. IPSS-M scores ranged from –1.61 to 4.39 (median=0.285); cases were subclassified by risk class into
96 Very Low (n=1), Low (n=6), Moderate Low (n=7), Moderate High (n=3), High (n=5), and Very High (n=10).

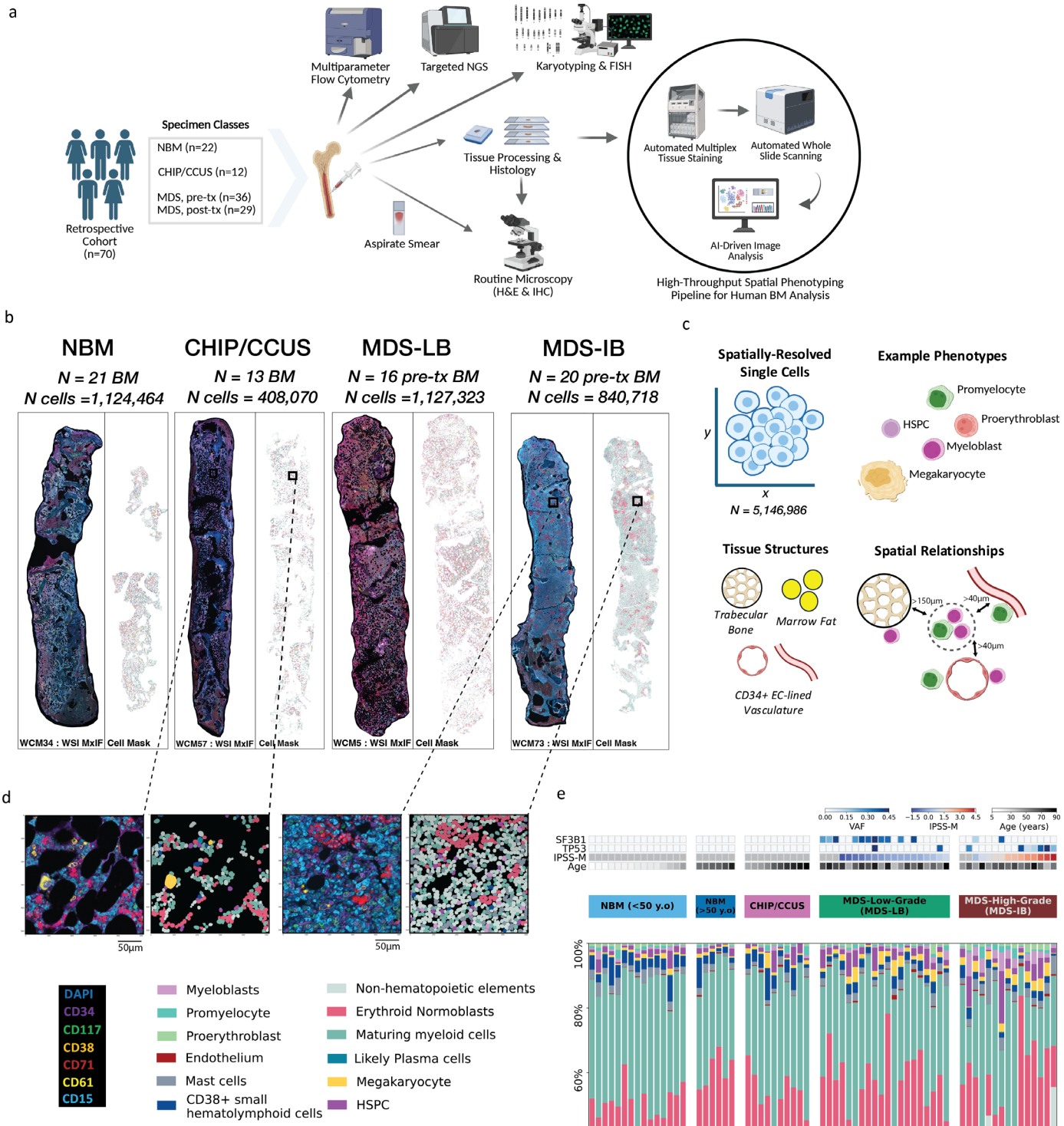

f

Group Label	BM Core Biopsy Number of Samples	Cells Phenotyped	Total Tissue Region	Abundant Mutation	Serial Samples Clinical Follow-up
NBM (< 50 y.o)	N = 15 cases	852,385	124.35 mm²		
NBM (> 50 y.o)	N = 6 cases	272,079	37.92 mm²		
CHIP/CCUS	N = 13 cases	408,070	108.86 mm²		
MDS-LB	N = 20 pre-tx cases	1,127,323	298.90 mm²	11 SF3B1m	5 patients 8 post-tx core biopsy
MDS-IB	N = 16 pre-tx cases	840,718	230.62 mm²	7 TP53m	9 patients 21 post-tx core biopsy

Figure 1. MDS Bone marrow trephine biopsy whole-slide imaging cohort and single-cell spatial analysis. a, Bone marrow trephine biopsy data collection schematic (designed with BioRender). **b,** Whole-slide multiplexed-immunofluorescence image examples and single-cell level phenotyped segmentation maps for sample groups in treatment-naive cohort**.** MDS patients are divided broadly into low blast (MDS-Low-Grade/MDS-LB) and high blast (MDS-High-Grade/MDS-IB) sample groups. Non-MDS samples categorized as clonal hematopoiesis of indeterminate potential/clonal cytopenia of undetermined significance (CHIP/CCUS), normal bone marrow (NBM; <50yrs or ≥50yrs). **c,** Diagram of features collected for downstream analysis (designed with BioRender). **d,** Side-by-side visualization of immunofluorescence image ROI and cell phenotyped segmentation map derived from two example cases. Legend of antibody color channel assignments and cell phenotype classifications. **e,** Variations in cell type proportions across entire treatment-naïve cohort. 12 cell types defined using membrane marker phenotypes and morphologic parameters. **f,** Table of sample sizes for each sampled group. Values shown are sample group label, number of cases, total cells phenotyped, total tissue region, abundant mutation for disease groups, and number of serial samples collected as part of treatment cohort.

97 ***Quantitative and morphologic variations between normal and MDS bone marrows***

98 Following multiplex immunofluorescence (MxIF) staining and whole slide imaging (WSI) of trephine
99 biopsy tissues, individual cells and architectural structures were segmented and further characterized as
100 previously described, resulting in a dataset of 5,146,986 phenotyped and spatially-resolved single cells (**Figure**
101 **1b-f, Supplementary Data Figure 1a-b**).[11]

102 Quantification of various hematopoietic cell types by MxIF analysis, including myeloblasts,
103 promyelocytes, erythroid normoblasts, and maturing myeloid cells (MMCs), correlated positively with orthogonal
104 measurements using conventional methods (e.g. manual cell counting, multiparameter flow cytometry [MFC]-
105 based immunophenotyping) (**Supplementary Data Figure 1c, Supplementary Data Table 2**).

106 MxIF analysis further revealed differences in proportions of several rare cell types between NBMs, and
107 treatment-naïve samples from the pathologic subgroups CHIP/CCUS, MDS-LB, and MDS-IB [**Figure 2**].

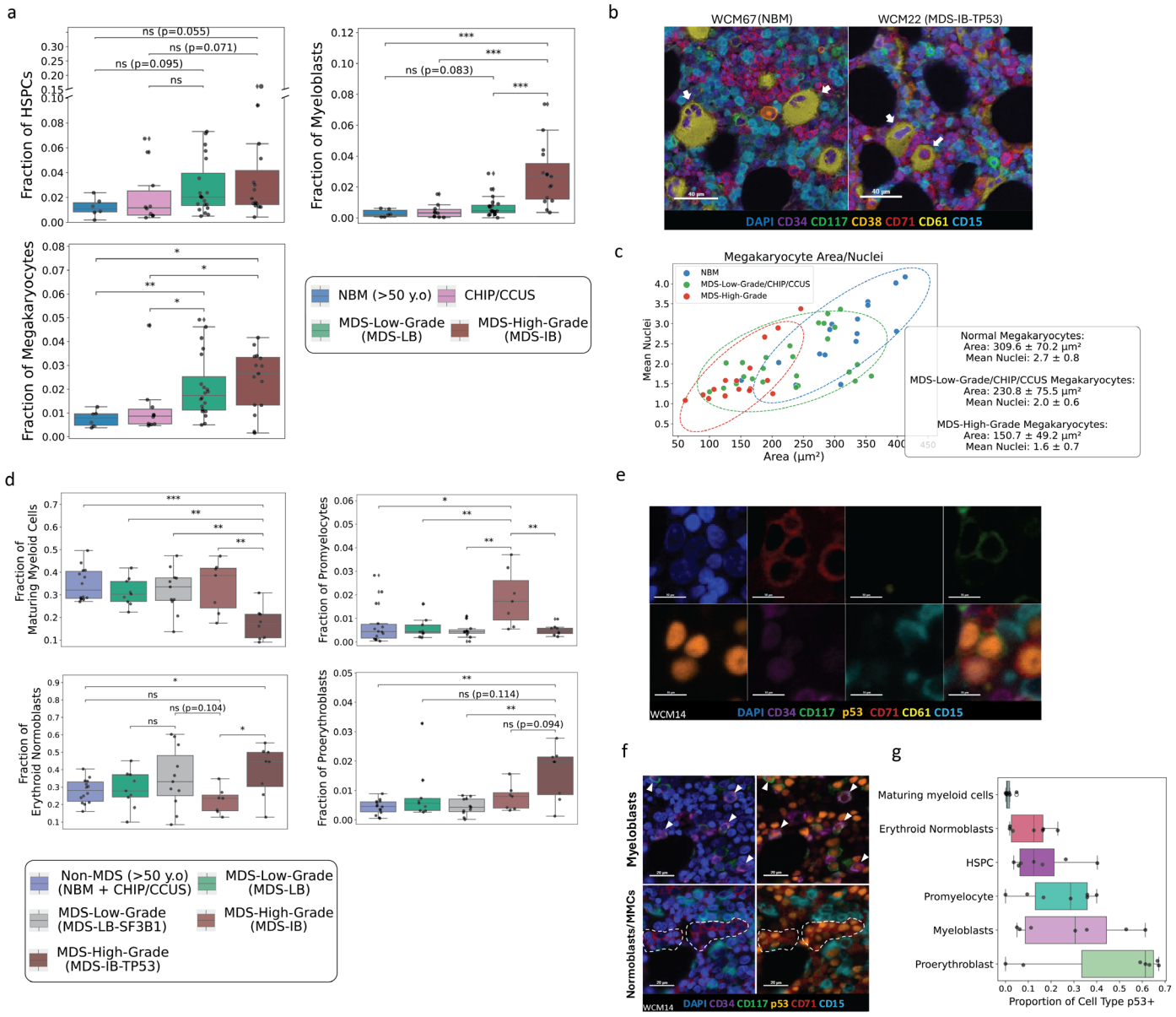

Figure 2. Single-cell proportional and morphologic changes in MDS. a, Comparison of HSPC, myeloblast, and megakaryocyte proportions across primary sample groups (Mann-Whitney U-test; *p≤0.05, **p≤0.01, ***p≤0.001). **b**, Representative MxIF images from NBM and MDS samples showing significant differences in megakaryocyte size/morphology. **c,** Quantification of mean megakaryocyte cell area and number of nuclei across progression from NBM to high grade MDS samples shown as scatter plot with standard deviation values drawn as ellipses between NBM, CHIP/CCUS and MDS-LB, and MDS-IB. **d,** Comparison of maturing myeloid cell (MMC), promyelocyte, proerythroblast, and erythroid normoblast proportions across sample groups, with additional MDS-IB stratification by *TP53* mutation status (Mann-Whitney U-test; *p≤0.05, **p≤0.01, ***p≤0.001). **e,** Representative MxIF image of putative *TP53*-mutated myeloblasts and erythroid normoblasts based on high p53 expression. **f,** A

representative cluster of putative *TP53*-mutated CD117+CD71+ proerythroblasts is shown (case WCM14). Top row (left to right): DAPI (blue), CD71 (red), CD61 (yellow), CD117 (green); bottom row: p53 (orange), CD34 (magenta), CD15 (cyan), Merge. **g,** Proportions of cells identified with high p53 protein expression across all MDS-*TP53* samples in tissue microarray. The proportion value on the x-axis is calculated as the number of p53+ cell type instances divided by total number of cell type instances. All MxIF images shown captured with Phenochart (v1.1, Akoya Biosciences).

108 The proportions of HSPCs, myeloblasts, and megakaryocytes increased commensurate with disease
109 severity (**Figure 2a, Supplementary Data Figure 2a**); HSPC compartment expansion in MDS patients has been
110 previously demonstrated using MFC performed on aspirated marrow samples.[12] Interestingly, we found that the
111 increased frequency of megakaryocytes in MDS-IB cases was accompanied by an increase in small, frequently
112 mononuclear forms, and quantification of megakaryocyte nuclei and cell area confirmed this (**Figure 2b-c**).
113 Megakaryocytes expressing CD34 could be found in all sample groups and were consistently smaller than CD34-
114 negative megakaryocytes (**Supplementary Data Figure 2d);** of note, MDS-IB-*TP53* samples contained the
115 greatest proportions of CD34+ megakaryocytes. Erythroid normoblast cell areas were significantly larger in both
116 MDS groups compared to age-matched NBMs and CHIP/CCUS samples **(Supplementary Data Figure 2e).**
117 Interestingly, the sizes of proerythroblasts and promyelocytes correlated inversely with IPSS-M scores, with the
118 smallest of these cell types found in *TP53*-mutated samples **(Supplementary Data Figure 2f).**

119 In subgroup analyses, MDS cases harboring *TP53* mutations were characterized by the most significant
120 depletions in promyelocytes and MMCs, but the most significant increases in proerythroblasts and maturing
121 erythroid normoblasts, particularly when compared to other MDS-IB samples (**Figure 2d**). We found no
122 significant differences in the proportions of endothelial cells between all sample groups (**Supplementary Data**
123 **Figure 2b**).

124 p53 protein labeling has been well-described as a method for identifying mutant p53 protein-containing
125 cells (putative *TP53*-mutated cells) in tissue sections.[13–15] By integrating this with MxIF, we identified enrichment

126 of *TP53*-mutated cells within the myeloblast, proerythroblast, and erythroid normoblast compartments (**Figure**
127 **2e-g**, **Supplementary Data Figure 2c**).

128 ***HSPCs and early hematopoietic progenitors are progressively displaced from perivascular and para-trabecular***
129 ***zones along progression from clonal hematopoiesis to overt MDS***

130 We previously demonstrated in NBMs that HSPCs are consistently localized proximal to bone trabeculae
131 and CD34+ endothelial cell-lined vasculature in both younger and older individuals.[11] However, HSPCs appeared
132 displaced in MDS samples, prompting us to investigate further using permutation testing (**Figure 3a-b**). HSPCs
133 were found proximal (within 15µm) to vasculature in young and old NBMs, and in CHIP/CCUS samples, but
134 displaced in both MDS-LB and MDS-IB samples (**Figure 3c-d, Supplementary Data Figure 3a-b)**. Assessment
135 of sample-level data revealed that roughly half of MDS-LB and MDS-IB samples lacked evidence of HSPC
136 localization near vasculature; additionally, nearly all MDS-LB and MDS-IB samples lacked evidence of peri-
137 vascular myeloblast localization (**Supplementary Data Figure 3a**). Distance analysis further indicated that
138 HSPCs were located at greater distances from vasculature than other cell types within samples in MDS cases
139 (**Supplementary Data Figure 3b**). Myeloblasts exhibited a perivascular exclusionary pattern similar to HSPCs,
140 while other early granulocyte- (promyelocytes) were only found to be significantly displaced in MDS-IB (**Figure**
141 **3c, Supplementary Data Figure 3a**). Conversely, CD38+ small hematolymphoid cells and megakaryocytes were
142 consistently found proximal to vasculature in all sample groups, with megakaryocytes demonstrating a strong
143 relative enrichment pattern in MDS samples (**Figure 3c, Supplementary Data Figure 3a-b**). We have previously
144 dissected mechanisms underlying perivascular niche localization and consequent maturation and function of
145 megakaryocytes,[16] although it remains to be explored whether these pathways are fully maintained in the setting
146 of MDS. Of note, erythroid normoblasts were negatively enriched with respect to endothelium in all groups
147 (**Supplementary Data Figure 3a**). Collectively, these data indicate a remodeling of the immediate perivascular
148 cell composition in MDS samples relative to NBMs (**Figure 3d**).

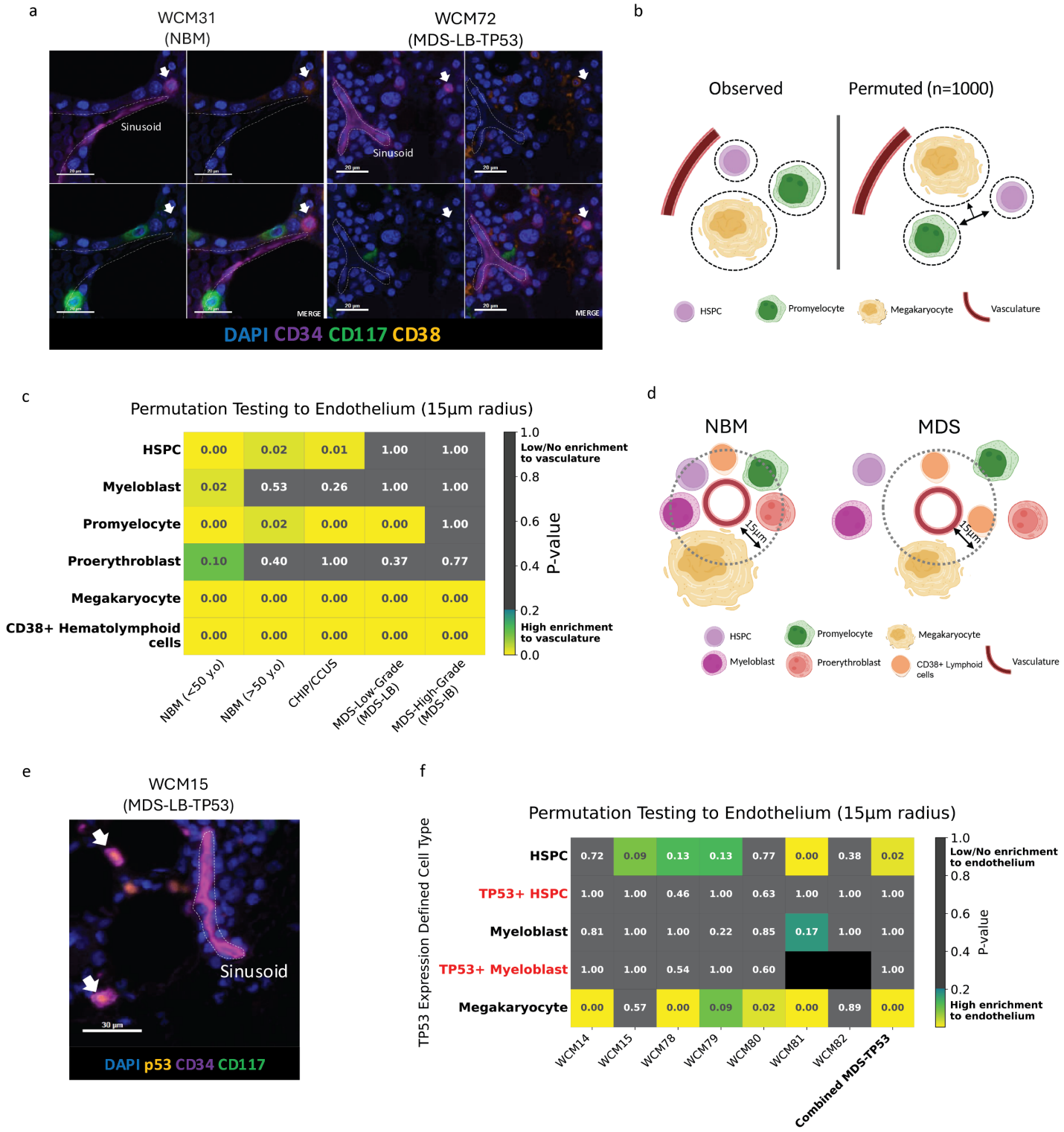

Figure 3. HSPCs and early hematopoietic progenitors are progressively displaced from perivascular zones along progression from clonal hematopoiesis to overt MDS. a, Representative MxIF images of HSPC localization to (NBM) and displacement from (MDS) vasculature. **b,** Permutation testing spatial analysis metagraphical schematic (designed with BioRender).

c, Heatmap with p-values combined across sample groups (Stouffer's method) representing the significance of cell type localization to vasculature within 15µm radius. Lower values (yellow) indicate significant spatial enrichment (cells closer to endothelium) as compared with randomly generated distribution, and higher values (gray) represent the lack of enrichment (cells further away/displaced from endothelium). **d,** Cartoon schematic representing altered cellular composition in the perivascular niche as measured by permutation testing and other distance-based analysis observed in NBM versus MDS cases (designed with BioRender). **e,** Representative MxIF image of *TP53*-mutated MDS sample showing HSPCs with high p53 expression (putative *TP53*-mutated HSPCs) displaced from endothelium. **f,** Permutation testing heatmap computed on tissue microarray cohort between cell type categories sub-defined by p53 expression. Low p-values (yellow) indicate significant association with endothelium as compared with high p-values (gray) indicating displacement from endothelium.

149 We next investigated whether perivascular enrichment patterns differed between wild-type and clonal
150 HSPCs, by again using p53 protein labeling to distinguish *TP53*-mutant from -WT HSPCs **(Figure 3e).**
151 Remarkably, we found WT-HSPCs localized more closely with endothelial cells, whereas *TP53*-mutated HSPCs
152 were significantly displaced from endothelium (**Figure 3e-f, Supplementary Data Figure 3e**). This finding
153 suggests that clonal HSPCs specifically drive the observed "global" pattern of HSPC displacement from
154 perivascular regions, particularly in *TP53*-mutated samples.

155 To investigate a mechanism for displacement of HSPCs from vasculature, we searched publicly available
156 gene and protein expression datasets of MDS patient samples for possible interactomes between HSPCs and
157 endothelial cells. Previous studies have shown the importance of secreted CXCL12 in inducing migration to the
158 bone marrow niche of CXCR4-expressing HSPCs. CXCL12 can be expressed by endothelial cells and
159 perivascular stromal cells,[17] and increased CXCL12 levels have been reported in MDS although, notably, HSPCs
160 from MDS samples exhibit significantly reduced migration toward CXCL12 in vitro.[18,19]

161 Based on re-analysis of publicly available RNA sequencing and surface protein expression datasets,[18,20–
162 22] we found consistently reduced CXCR4 gene and protein expression within HSPC compartments from MDS
163 samples, relative to healthy controls **(Supplementary Data Figure 4).** Notably, *CXCR4* was the only significantly

164 downregulated gene within HSPC populations across four RNA sequencing datasets **(Supplementary Data**
165 **Figure 4d**).

166 As we previously reported in NBMs, HSPCs, myeloblasts, and promyelocytes also exhibited consistent
167 significant localization to para-trabecular regions in CHIP/CCUS samples **(Supplementary Data Figure 3c-d).**
168 In contrast to their displacement from vasculature, HSPC localization to trabeculae was mostly conserved in MDS
169 samples regardless of disease severity or genotype; average distance measurements and permutation score
170 analysis revealed that the distance from HSPCs to trabeculae increases in MDS-LB and MDS-IB samples,
171 although in the majority of samples HSPCs remain more significantly enriched than other hematopoietic cell
172 types **(Supplementary Data Figure 3c-d)**. Conversely, assessment of these same statistics for myeloblasts and
173 promyelocytes indicated a widespread disruption of normal localization of these cells to trabeculae in a large
174 portion of MDS-LB and MDS-IB samples (**Supplementary Data Figure 3c-d**).

175 ***Atypical erythroid island formation in MDS***

176 While erythroid normoblasts are normally found in well-formed maturation "islands" in NBMs,
177 disaggregation of these structures is a recognized phenomenon and can be appreciated by light microscopy in
178 MDS bone marrow tissues, particularly when the disease is advanced.[23–26]

179 Indeed, we could visualize larger well-formed erythroid aggregates in NBMs, with conspicuous
180 disaggregation in MDS-IB samples (**Figure 4a**)**.** However, robust quantification of this phenomenon, especially
181 at earlier stages of the disease, and correlation with clinical status and/or underlying genetics has not been
182 previously described. Using whole level-slide erythroid normoblast phenotype maps, we could visualize differing
183 aggregation patterns between NBM/CHIP/CCUS and MDS samples **(Figure 4b, Supplementary Figure 5a)**. At
184 both the single-cell and sample levels, we found a larger distance between an erythroid normoblast to its nearest
185 neighboring normoblast in MDS relative to NBM and CHIP/CCUS patients **(Figure 4c)**.

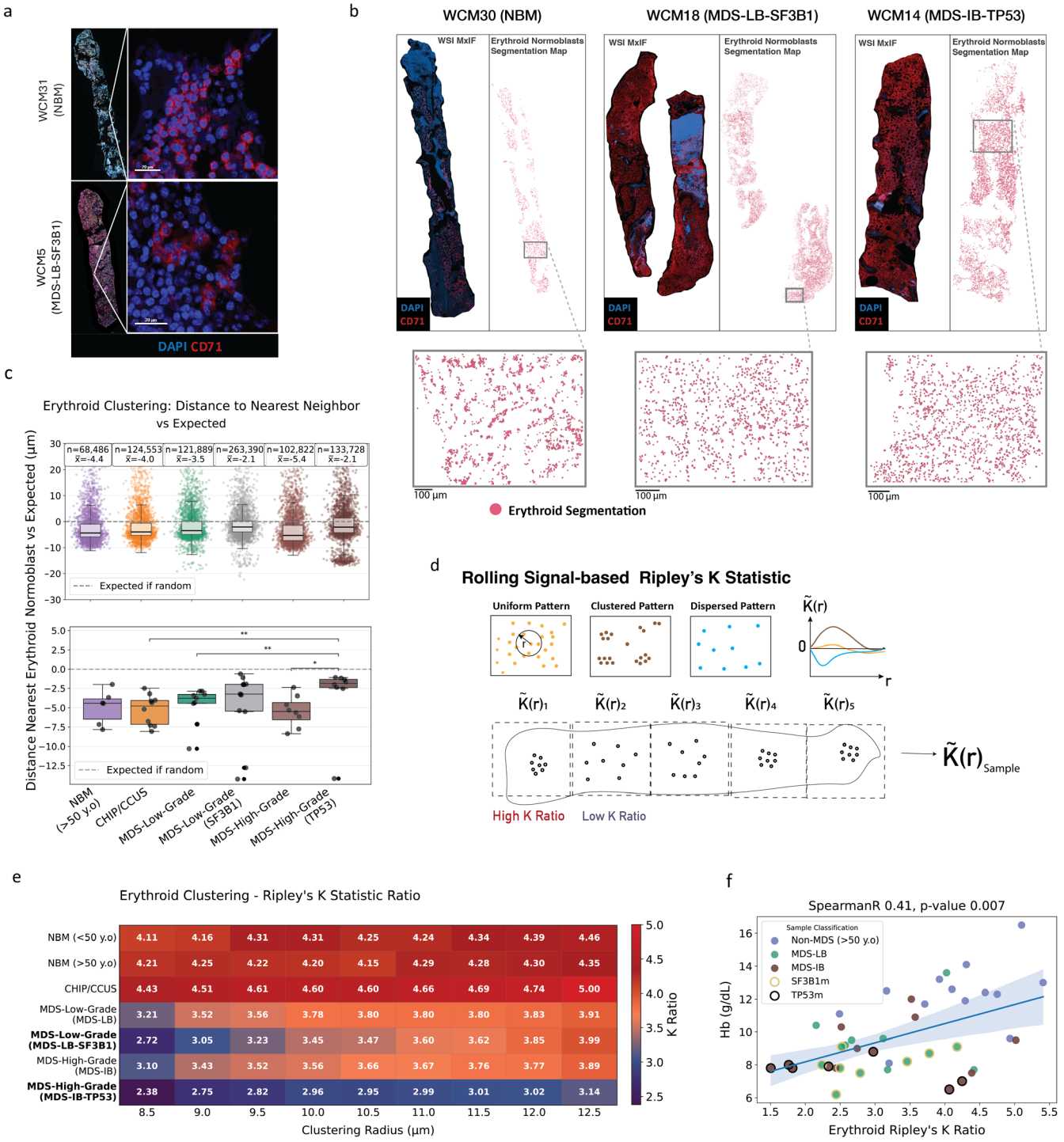

Figure 4. Atypical erythroid island formation in MDS. a, Representative image example with well-formed strongly aggregated erythroid island in an NBM sample (top) and disaggregated and sparsely arranged erythroid normoblasts in an MDS-LB-*SF3B1* sample (bottom) **b,** Whole-slide image displayed as merged DAPI and CD71 channels on left and mask of erythroid normoblast cell segmentations on the right for three representative cases in three sample groups: NBM, MDS-LB-*SF3B1*, MDS-IB-*TP53*. Below the image examples are zoomed-in ROIs of erythroid normoblast spatial clustering pattern. **c,** Box plot of single-cell

distribution (top) and sample distribution (bottom) of erythroid normoblast distance to nearest neighboring erythroid normoblast normalized by distance to all other cell types (Expected distance) [Mann-Whitney U-test; *p≤0.05, **p≤0.01, ***p≤0.001]. **d,** Schematic for testing Rolling Signal-based Ripley's K statistic (RSRK) across an entire WSI. **e,** Heatmap with mean (Rolling Signal-based) erythroid clustering K statistic between genotype sub-defined sample groups at multiple radii. MDS-LB-*SF3B1* and MDS-IB-*TP53* samples notably have low clustering values across radii (i.e., disaggregated spatial pattern). **f,** Regression line scatter plot shows Ripley K statistic clustering value has significant (Spearman R = .41; P = .007) positive trend with patient Hemoglobin CBC value across MDS and age-matched Non-MDS cohort. MDS-LB-*SF3B1* and MDS-IB-*TP53* samples are highlighted with yellow and black circles respectively, trending with the lowest Hemoglobin values and lowest erythroid clustering K statistics.

186 To further analyze these patterns across all treatment-naïve samples and evaluate for differences between
187 specimen classes, we employed Rolling Signal-based Ripley's K statistic, a method used to quantify the
188 aggregation of points in two-dimensional space within discrete radii **(Figure 4d).** Erythroid normoblasts were
189 found to have the highest K-ratios (i.e., greater clustering patterns), in NBMs at all tested radii; conversely, the
190 lowest K-ratios were observed in MDS-IB samples harboring *TP53* mutations (MDS-IB-*TP53*). However, MDS-
191 LB samples harboring *SF3B1* mutations (MDS-LB-*SF3B1*) were also characterized by lower K-ratios than
192 observed in *SF3B1*-WT/*TP53*-WT MDS-LB and MDS-IB samples (**Figure 4e**). Similarly, by erythroid cluster
193 density analysis, MDS-LB-*SF3B1* and MDS-IB-*TP53* samples were found to have the lowest density values
194 (**Supplementary Data Figure 5b-c**). These data suggest that erythroid island breakdown is a distinguishing
195 feature of MDS topography compared to NBMs, but moreover, the degree of distortion may be related to genotype
196 irrespective of histologic grade of disease. Interestingly, the K-ratio statistic correlated positively with peripheral
197 blood hemoglobin values, suggesting a relationship between poor erythroid island formation and anemia (**Figure**
198 **4f**).

199 ***Atypical localization of immature precursors (ALIP) correlates with disease severity and discriminates TP53-***
200 ***mutated and -WT subtypes of high-risk MDS***

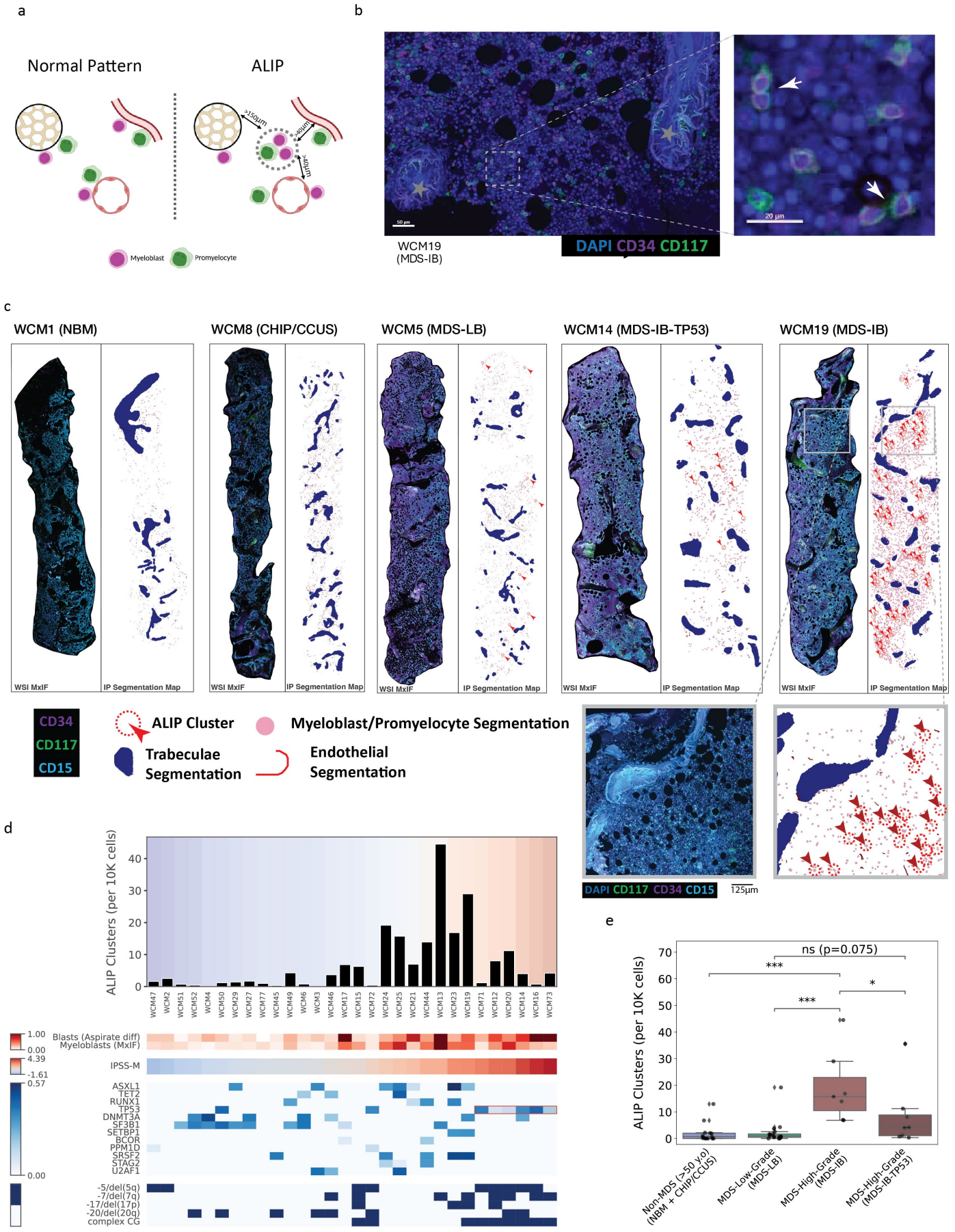
a
Normal Pattern
ALIP
>150µm
<40µm
<40µm
Myeloblast
Promyelocyte
b
WCM19
(MDS-IB)
DAPI CD34 CD117
50 µm
20 µm
c
WCM1 (NBM)
WCM8 (CHIP/CCUS)
WCM5 (MDS-LB)
WCM14 (MDS-IB-TP53)
WCM19 (MDS-IB)
WSI MxIF
IP Segmentation Map
CD34
CD117
CD15
ALIP Cluster
Trabeculae Segmentation
Myeloblast/Promyelocyte Segmentation
Endothelial Segmentation
DAPI CD117 CD34 CD15
125µm
d
ALIP Clusters (per 10K cells)
Blasts (Aspirate diff)
Myeloblasts (MxIF)
IPSS-M
ASXL1
TET2
RUNX1
TP53
DNMT3A
SF3B1
SETBP1
BCOR
PPM1D
SRSF2
STAG2
U2AF1
-5/del(5q)
-7/del(7q)
-17/del(17p)
-20/del(20q)
complex CG
e
ALIP Clusters (per 10K cells)
ns (p=0.075)
***
***
*
Non-MDS (>50 y.o)
(NBM + CHIP/CCUS)
MDS-Low-Grade
(MDS-LB)
MDS-High-Grade
(MDS-IB)
MDS-High-Grade
(MDS-IB-TP53)

Figure 5. Atypical localization of immature precursors (ALIP) correlates with disease severity and discriminates *TP53*-mutated and -WT subtypes of high-risk MDS. a, Graphical schematic for determining ALIP clusters from myeloblast and promyelocyte co-localization in locations >150µm from trabeculae and >40µm from vasculature (designed with BioRender). **b,** Image example from MDS-IB case showing clusters of abnormally located immature precursors (ALIP) in BM tissue region distant from trabecular bone and endothelium. Arrows denote ALIP cluster observations in zoomed-in region. Star symbols annotate bone trabeculae. **c,** Whole-slide image examples shown as merged CD117, CD34, and CD15 channels (left) and segmentation maps of bone trabeculae (dark blue), endothelium (dark red), and myeloblast and/or promyelocyte segmentations (grey/pink circles). ALIP observations are annotated with red arrows in segmentation maps. Representative examples are shown for sample groups NBM, CHIP/CCUS, MDS-LB, MDS-IB-*TP53*, and MDS-IB. **d,** Bar plot with quantification of ALIP clusters at the sample level in MDS cases (normalized as frequency of ALIP clusters per 10,000 total nucleated cells in sample). Annotated in heatmaps below each bar for each sample are manual counting-based blast count from the aspirate smear, the sample level myeloblast proportion determined from MxIF quantification, IPSS-M risk score, variant allele frequency for selected mutated genes, and chromosomal abnormalities. **e,** MDS-IB samples show the highest frequencies of ALIP clusters (Mann-Whitney U-test; *$p \leq 0.05$, **$p \leq 0.01$, ***$p \leq 0.001$).

201 As shown in our recent work and confirmed in this study, the most immature granulocyte progenitors are
202 normally localized near bone trabeculae and vasculature in NBMs, with more mature progenitors enriched in
203 medullary areas of the bone marrow. Atypical localization of immature precursors (ALIP) is a histologic pattern
204 originally recognized in conventional hematoxylin and eosin-stained bone marrow tissue, and later confirmed by
205 single marker immunohistochemical studies, as abnormal clustering of myeloblasts and/or promyelocytes at
206 significant distances from bone and vasculature **(Figure 5a).**[27,28] Importantly, early studies correlated the presence
207 of ALIP with poor cytogenetic risk factors and inferior survival characteristics.[29] However, more detailed
208 assessments of ALIP have been lacking.

209 As expected, we identified foci of ALIP in a subset of MDS samples (**Figure 5b**, representative example).
210 To quantify this finding, we defined ALIP by the presence of two or more myeloblasts and/or promyelocytes
211 clustered within 12µm of each other at a distance >150µm from bone trabeculae and >40µm from endothelium.
212 Using whole slide-level image data, we could visualize variations in ALIP cluster frequency and distribution
213 between NBM, CHIP/CCUS and MDS samples (**Figure 5c)**.

214 Among treatment-naïve MDS samples, ALIP cluster density was lowest in MDS-LB samples and highest
215 in a large proportion of MDS-IB samples (**Figure 5d-e, Supplementary Data Figure 6**); this pattern was retained
216 when we corrected for sample cellularity or tested different cluster compositions and/or distance metrics.
217 However, notably, among MDS-IB samples ALIP cluster density was highest in *TP53*-wild-type higher risk cases
218 (**Figure 5d-e**). This finding provides additional evidence of genetically imprinted spatial heterogeneity in the
219 microarchitecture of MDS-IB cases that may appear homogeneous by IPSS-M-based risk assessment.

220 ***Integration of single cell quantitative features and microarchitectural patterns to generate a spatially informed***
221 ***Microarchitectural Perturbation Score (MAPS)***

222 We next aggregated all single cell-level and spatial pattern data into a composite parameter, which we
223 termed the "MDS Microarchitectural Perturbation Score" (MDS-MAPS), to analyze tissue samples at the whole-
224 slide and patch level (**Figure 6a**). Dimensionality reduction by t-distributed Stochastic Neighbor Embedding (t-
225 SNE) demonstrated essentially distinct clustering of NBMs and treatment-naïve MDS samples (**Figure 6b,**
226 **Supplementary Data Figure 7a**). Interestingly, MDS-LB and MDS-IB samples lacking *TP53* mutations
227 clustered similarly according to IPSS-M scores, while *TP53*-mutated MDS samples formed a completely distinct
228 group. Feature extraction analyses revealed multiple single cell parameters, spatial patterns, and marrow structural
229 characteristics as determinants of the observed t-SNE distributions **(Supplementary Data Figure 7c).** NBMs
230 were characterized by higher frequencies of CD38+ small hematolymphoid cells, HSPC enrichment near
231 vasculature, larger multi-nucleated megakaryocytes, and greater fat to cell ratio. Conversely, key parameters for
232 clustering of *TP53*-WT MDS samples were a higher proportion of myeloblasts and promyelocytes and ALIP
233 cluster instances. The distinct cluster of *TP53*-mutated MDS samples was driven by high proportions of
234 megakaryocytes and significant displacement of HSPCs and myeloblasts from within 15µm of vasculature.

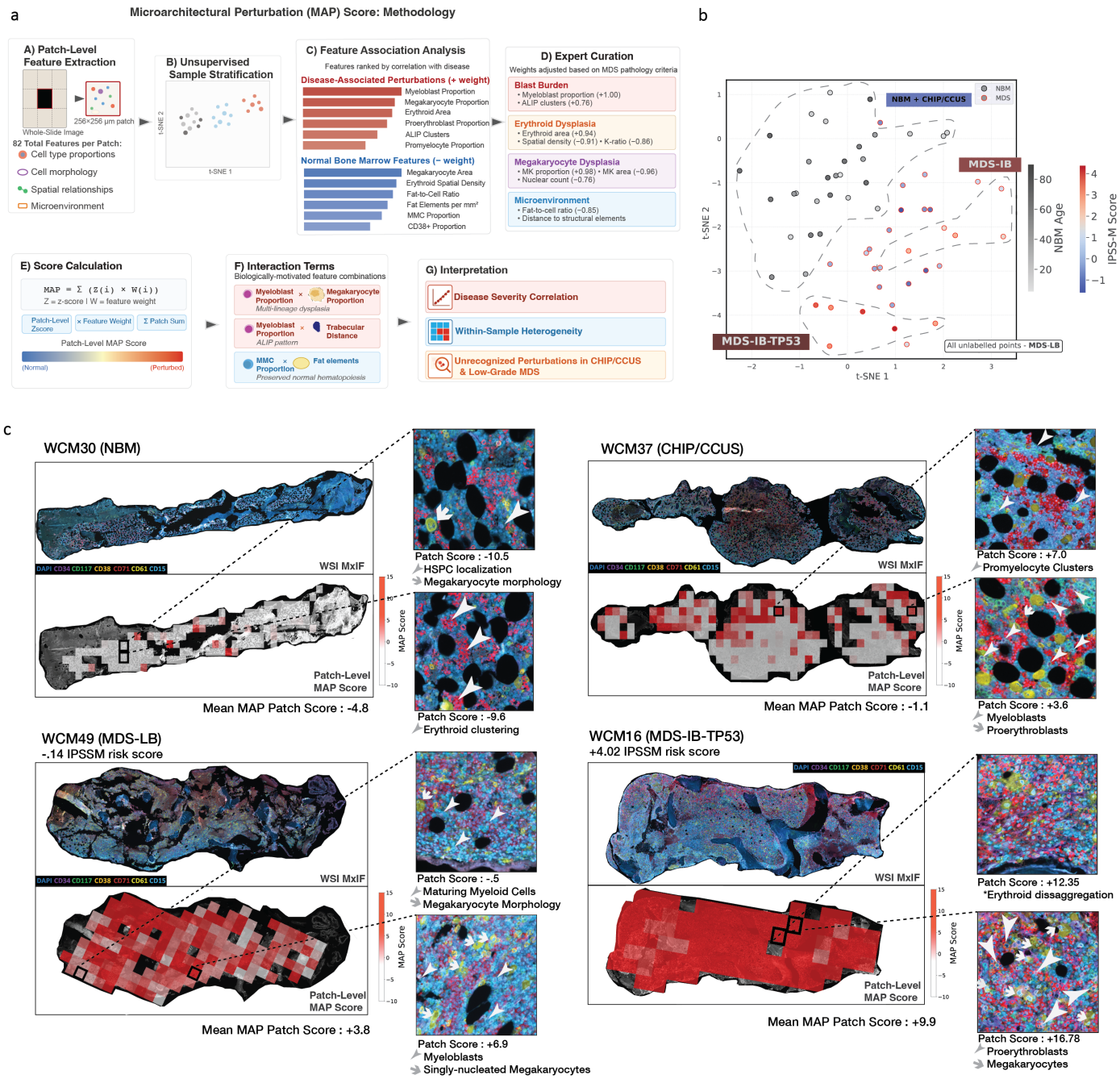
a
Microarchitectural Perturbation (MAP) Score: Methodology
A) Patch-Level Feature Extraction
256×256 µm patch
Whole-Slide Image
82 Total Features per Patch:
Cell type proportions
Cell morphology
Spatial relationships
Microenvironment
B) Unsupervised Sample Stratification
t-SNE 2
t-SNE 1
C) Feature Association Analysis
Features ranked by correlation with disease
Disease-Associated Perturbations (+ weight)
Myeloblast Proportion
Megakaryocyte Proportion
Erythroid Area
Proerythroblast Proportion
ALIP Clusters
Promyelocyte Proportion
Normal Bone Marrow Features (− weight)
Megakaryocyte Area
Erythroid Spatial Density
Fat-to-Cell Ratio
Fat Elements per mm²
MMC Proportion
CD38+ Proportion
D) Expert Curation
Weights adjusted based on MDS pathology criteria
Blast Burden
• Myeloblast proportion (+1.00)
• ALIP clusters (+0.76)
Erythroid Dysplasia
• Erythroid area (+0.94)
• Spatial density (−0.91) • K-ratio (−0.86)
Megakaryocyte Dysplasia
• MK proportion (+0.98) • MK area (−0.96)
• Nuclear count (−0.76)
Microenvironment
• Fat-to-cell ratio (−0.85)
• Distance to structural elements
E) Score Calculation
MAP = Σ (Z(i) × W(i))
Z = z-score | W = feature weight
Patch-Level Zscore
× Feature Weight
Σ Patch Sum
Patch-Level MAP Score
(Normal)
(Perturbed)
F) Interaction Terms
Biologically-motivated feature combinations
Myeloblast Proportion × Megakaryocyte Proportion
Multi-lineage dysplasia
Myeloblast Proportion × Trabecular Distance
ALIP pattern
MMC Proportion × Fat elements
Preserved normal hematopoiesis
G) Interpretation
Disease Severity Correlation
Within-Sample Heterogeneity
Unrecognized Perturbations in CHIP/CCUS & Low-Grade MDS
b
NBM + CHIP/CCUS
NBM
MDS
MDS-IB
MDS-IB-TP53
All unlabelled points - MDS-LB
t-SNE 2
t-SNE 1
NBM Age
IPSS-M Score
c
WCM30 (NBM)
WSI MxIF
Patch-Level MAP Score
Mean MAP Patch Score : -4.8
Patch Score : -10.5
HSPC localization
Megakaryocyte morphology
Patch Score : -9.6
Erythroid clustering
WCM37 (CHIP/CCUS)
Mean MAP Patch Score : -1.1
Patch Score : +7.0
Promyelocyte Clusters
Patch Score : +3.6
Myeloblasts
Proerythroblasts
WCM49 (MDS-LB)
-.14 IPSSM risk score
Mean MAP Patch Score : +3.8
Patch Score : -.5
Maturing Myeloid Cells
Megakaryocyte Morphology
Patch Score : +6.9
Myeloblasts
Singly-nucleated Megakaryocytes
WCM16 (MDS-IB-TP53)
+4.02 IPSSM risk score
Mean MAP Patch Score : +9.9
Patch Score : +12.35
*Erythroid dissaggregation
Patch Score : +16.78
Proerythroblasts
Megakaryocytes
MAP Score
d
Patch-Level MAP Score
Mean Patch-Level MAP Score
NBM (>50 y.o)
CHIP/CCUS
IPSS-M Score
e
Mean MAP Score
Sample-Level Entropy
Non-MDS (>50 y.o) (NBM + CHIP/CCUS)
MDS-Low-Grade (MDS-LB)
MDS-High-Grade (MDS-IB)
MDS-High-Grade (MDS-IB-TP53)
ns
***
**
*

Figure 6. Integration of single cell quantitative features and microarchitectural patterns to generate a spatially-informed MDS Microarchitectural Perturbation Score (MDS-MAPS). a, Schematic illustrating methodology for deriving and calculating MDS-MAPS. Schematic details extracting patch-level features, deriving feature importance, and calculating perturbation score in additive model at the 256x256µm patch level. **b,** t-Distributed Stochastic Neighbor Embedding **(**t-SNE) dimensionality reduction plot of sample level data showing unique clustering pattern of MDS-IB and MDS-IB-*TP53* samples in distant groups from NBM and clonal hematopoiesis samples. NBM samples are scaled in color by age; MDS samples are scaled in color by IPSS-M risk score. **c,** Representative WSI examples of bone marrow core biopsy samples as MxIF (top) and heatmap rendering (bottom) of patch-level MDS-MAPS. Shown are four cases from sample groups NBM, CHIP/CCUS, MDS-LB, MDS-IB-*TP53*. White patches are quantified as low MDS-MAPS (normal), red patches are quantified as high MDS-MAPS (perturbed). Representative 256x256µm patch MxIF images, with dotted lines drawn from location in WSI, are shown and labeled with features contributing to patch-level score. **d,** Bar plot with samples on the x axis and mean MDS-MAPS by sample on the y axis. Samples colored in grey are in NBM/CHIP/CCUS sample groups; MDS samples are color coded by IPSS-M score according to color bar. **e,** Box plot and statistical comparison for mean MDS-MAPS (left) and sample-level entropy of MAPS values (right) (Mann-Whitney U-test; *$p \leq 0.05$, **$p \leq 0.01$, ***$p \leq 0.001$).

To investigate whether disease-related perturbations were uniform or heterogenous within tissue samples, we next computed single-cell morphologic features, cell phenotype proportion, spatial relationships and microenvironmental localization locally at the 256µm square patch level; this amounted to 82 patch-level features. Dimensionality reduction of patch-level observations revealed similar distinct clustering of *TP53*-mutated MDS patches from those extracted from NBM/CHIP/CCUS, and *TP53*-WT MDS samples **(Supplementary Data Figure 7b)**. MDS-MAPS was computed as a weighted score of patch-level observations, where weights were derived from sample-level disease severity stratification **(Supplementary Figure 7c)**. Using heatmaps overlaid on MxIF WSIs we compared MDS-related microarchitectural alterations between samples, and visualized local features contributing to varying MDS-MAPS scores at the patch level **(Figure 6c)**.

A heatmap analysis of patch-level MDS-MAPS in individual treatment-naïve samples revealed intra-tissue heterogeneity. Mean MDS-MAPS, the average of patch-level scores in each sample, generally increased commensurate with MDS grade, with the highest scores observed in *TP53*-mutated MDS samples **(Figure 6d-e Supplementary Figure 7d).** Interestingly, although MDS-MAPS values were aligned for most patients defined

248 as lower risk by IPSS-M (values <0), we identified discordant MDS-MAPS values (i.e., >0) in 7 of 13 patients
249 [WCM6, WCM27, WCM29, WCM49, WCM50, WCM51, WCM77]. Further examination of these cases revealed
250 features commonly identified in higher risk samples. Notably, MDS-LB samples were characterized by the
251 highest sample-level entropy in patch-level severity scores (**Figure 6e**), indicating underappreciated spatial
252 heterogeneity in microarchitectural perturbations found in MDS bone marrows, particularly at earlier stages of
253 disease. Indeed, we also identified focal high MDS-MAPS patches, characterized by noticeable features of
254 aberrant hematopoiesis, in samples from CHIP/CCUS patients, which we hypothesize could represent very early
255 stages of disease elusive to detection using conventional diagnostics.

256 ***Correlation of cell morphologic and spatial features with blast progression***

257 Although histomorphologic assessment of a bone marrow biopsy is required for diagnosis of MDS, blast
258 enumeration has remained the only parameter included in clinical prognostication models (e.g. IPSS-R, IPSS-
259 M).[5,6] Therefore, we developed a machine learning pipeline optimal for small sample sizes to determine whether
260 any of our extracted morphologic and spatial parameters could be associated with increased risk, or be considered
261 protective, with respect to blast count increases in patients receiving DMTs (n=16) [**Supplementary Data Table**
262 **3**]**.** The results of this exploratory analysis suggested that key MxIF parameters we found to be MDS-associated
263 have feature importance estimations of risk for disease progression, while NBM-like features have estimations as
264 protective, with considerable weight in the model alongside IPSS-M risk score **(Supplementary Data Figure**
265 **8a-b)**.

266 These findings suggest that histomorphologic features, particularly quantifiable spatial parameters
267 unidentifiable by routine microscopic evaluation, may be relevant for predicting disease evolution and have
268 additive value (i.e., to conventional blast enumeration) for risk assessment as currently performed using metrics
269 such as the IPSS-M.

270 ***Multimodal longitudinal assessment in the course of disease modifying therapies***

271 Longitudinal samples were analyzed for a subset of patients (n=14) who were treated with some
272 combination of growth factor therapy and hypomethylating agents, with or without venetoclax; three patients
273 received allogeneic stem cell transplantation. Among patients who only received pharmacologic agents, only three
274 achieved clinical remission during their treatment course (WCM2, WCM13, WCM44). A comprehensive
275 assessment of single cell morphologic and spatial parameters in longitudinal samples revealed an NBM-like
276 profile, with abrogation of various MDS-associated features, in bone marrow samples obtained at the time of
277 transient clinical and molecular-cytogenetic remission **(Figure 7a).** Notably, features indicating reversion to an
278 NBM-like profile were also observed in post-transplant samples from patients who received HSCT (WCM17,
279 WCM21, WCM46) **[Supplementary Data Figure 9].** By contrast, we did not observe similar changes in serial
280 samples from patients with *TP53*-mutated MDS (**Supplementary Data Figure 10**).

281 Assessment of serial samples from patients WCM13 and WCM44 illustrate how resolution of
282 microarchitectural alterations can be detected at the time of transient clinical and genetic disease remission
283 **(Figure 7a).** Both patients were characterized by high mean patch-level MDS-MAPS at diagnosis and initially
284 following therapy, with negative values concurrent with evidence of clinical and genetic remission **(Figure 7a**).
285 t-SNE analysis revealed that remission samples embedded more closely with NBM samples **(Figure 7b**).
286 Interestingly, in patient WCM44, for whom we analyzed seven serial biopsy samples, we observed transient re-
287 localization of HSPCs to vasculature at the time of clinical/genetic disease remission (**Figure 7c**). By evaluating
288 additional individual parameters, we identified higher ALIP cluster density, lower erythroid clustering K ratios,
289 larger erythroid normoblast areas, and larger megakaryocyte cell areas in samples at the time of active disease
290 relative to those collected at the time of remission (**Figure 7d)**.

291

292 **DISCUSSION**

293 The microarchitecture of hematopoiesis in the bone marrow remains relatively poorly understood.[30]
294 Although recent seminal studies using novel in situ imaging methods have begun to unravel the spatial anatomy
295 of murine hematopoiesis under steady-state and stress conditions,[31,32] achieving a similar understanding of the

human system has posed significant challenges. Novel approaches are critically needed to study intact bone marrow architecture in homeostatic and altered states, perhaps chief among them, MDS.

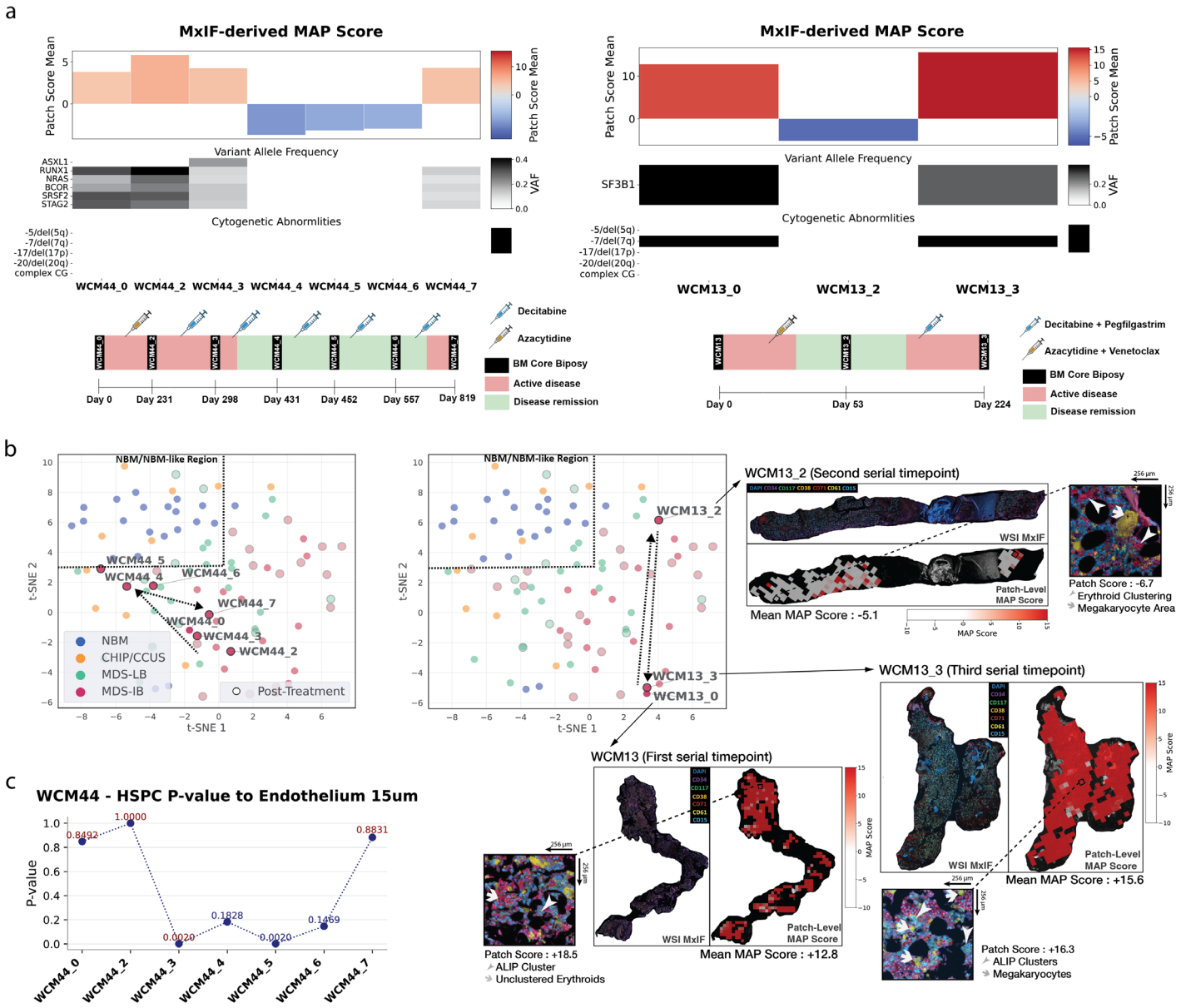

Figure 7. Multimodal longitudinal assessment in the course of disease modifying therapies. a, Bar plots displaying MDS-MAPS values quantified from bone marrow core biopsies at serial timepoints during disease management for two patients WCM44 (left) and WCM13 (right) that experienced transient remission. Overlayed under MAPS value bars are genetic mutations and cytogenetic alterations at each timepoint. Patient management timeline schematics are illustrated under bar plots with treatments between timepoints annotated with syringe symbols. Red color bars in timeline schematic indicate active disease; green color bar value in timeline schematic indicates disease remission. **b,** t-SNE plots for patients WCM44 (left) and WCM13 (right) traces case samples along the trajectory of disease treatment against sample-level embeddings of all Non-MDS and MDS samples. Post-treatment samples are highlighted with black circles. Region enriched in Non-MDS cases is drawn and annotated in top left corner. Bone marrow core biopsy WSIs and MDS-MAPS heatmaps at each timepoint are shown for case WCM13 with arrows pointed from the sample embedding on t-SNE plot. **c,** Line plot for patient WCM44 showing assessment of HSPC spatial enrichment to endothelium as a permutation testing p-value (high value indicates low/no enrichment, low value indicates significant HSPC localization to endothelium) along treatment course. **d,** Box plots of sample-level quantifications of individual features compared between active disease and remission samples in the two patients shown (WCM44 and WCM13). Dots are color-coded by patient.

298 Recently, we developed a method to study the microarchitecture of human hematopoiesis at single cell
299 resolution using automated whole slide immunofluorescence-based imaging of human trephine biopsy tissues
300 coupled with AI-based image analysis.[11] This method uses a panel of 6 antibodies and DAPI, which enables a
301 high-throughput classification of 12 hematopoietic cell types within the spatial context of the intact marrow. Our
302 initial studies demonstrated a largely consistent spatial organization of key hematopoietic cell types throughout
303 aging, with few architectural changes. Here, we aimed to address the nature and significance of perturbations in
304 MDS in order to advance clinical assessment. Inclusion of serial bone marrow samples collected from patients
305 treated using standard-of-care pharmacologic agents also permitted longitudinal tracking of microarchitectural
306 changes, revealing key features with additional prognostic and disease monitoring potential.

307 We found that MDS is marked by an increase in hematopoietic stem and progenitor cells (HSPCs), early
308 myeloid-committed progenitors (myeloblasts), and megakaryocytes, with this pattern intensifying as disease
309 severity increases. Notably, MDS samples with *TP53* mutations show significant differences in proportions of
310 erythroid and granulocytic progenitors, suggesting genotype-specific perturbations within hematopoietic

311 lineages. Cytomorphological analysis revealed that megakaryocytes, typically large and multi-nucleated in
312 normal bone marrow (NBM), become progressively smaller and mono-nucleated in MDS, correlating with other
313 features of increasing disease severity. Of note, it has been widely reported that megakaryocytes are key
314 components of the bone marrow niche and function through paracrine modulation of HSPC proliferation or
315 erythropoiesis.[33,34] Importantly, we observed the most significant megakaryocyte abnormalities in patients with
316 *TP53*-mutated MDS.

317 Our AI-based method was readily able to corroborate many of the typical changes in the hematopoietic
318 compartment identified using standard approaches (e.g. differential cell counting, flow cytometry) [**Figure 1a,**
319 **Supplementary Figure 1c**]; however, these conventional approaches lack the capacity to dissect architectural
320 changes. Our previous studies revealed that HSPCs are typically localized near trabecular bone and CD34-positive
321 endothelial cells in NBM, supporting prior work that has shown HSPCs to be perisinusoidal.[35] Here, we found
322 that HSPCs and myeloblasts are displaced from their perivascular location in MDS, while megakaryocytes and
323 putative B-cell precursors remain largely unaffected.

324 The significance of endothelial cells in governing bone marrow hemostasis was initially described over
325 twenty years ago,[36,37] and has been the subject of extensive research.[38,39] Our group has demonstrated the
326 modulatory role of endothelial cells through secretion of angiocrine factors that enable fine-tuned
327 thrombopoiesis,[16] stem cell self-renewal,[40] regeneration of hematopoiesis following injury,[41] and balancing the
328 fate of HSPCs.[42] The key architectural changes in the perivascular niche in MDS that we report in this study may
329 be drivers of the clinical manifestations of the disease.

330 The quest for a molecular basis to explain observed HSPC displacement from endothelium led us to
331 hypothesize that MDS HSPC's may be displaced from endothelium as a result of an altered CXCL12-CXCR4
332 axis. Using several publicly available datasets,[18,20–22] we found significantly and reproducibly lower CXCR4 gene
333 and protein expression in MDS HSPCs compared to healthy controls. Additionally, given that p53 has been shown
334 to participate in the modulation of CXCR4 levels,[43] it is not surprising that we found significant displacement of

335 *TP53*-mutated HSPCs from endothelium as compared to their wild-type counterparts. Moreover, this finding
336 points to a potential link between hematopoietic cell-intrinsic genetic defects and altered bone marrow
337 architecture.

338 Historical studies have identified abnormal architectural features in MDS, such as disrupted erythroid
339 islands and abnormal progenitor cell clustering,[23,27] though comprehensive characterization of these alterations
340 has been lacking. Our analyses confirmed reduced erythroid cluster density in MDS, but surprisingly, lower
341 cluster density was not exclusive to high-grade disease (e.g., *TP53*-mutated), as prominent erythroid island
342 disruption was also a feature of low-grade *SF3B1*-mutated samples. Although the precise role of SF3B1 in
343 establishing erythroid island architecture remains unknown, its role in erythropoiesis is well-recognized. Proper
344 erythroid differentiation requires efficient SF3B1-dependent mRNA splicing,[44] while mutation-associated mis-
345 splicing of key targets results in anemia.[45,46] Similarly, our observation of unique patterns of early progenitor cell
346 clustering (ALIP) in MDS-IB patients with or without *TP53* mutations further suggest a link between genotype
347 and microarchitecture.

348 To further quantify these microarchitectural changes, we combined single-cell and spatial data to generate
349 an "MDS Microarchitectural Perturbation Score" (MDS-MAPS). In an analysis of treatment-naive samples, MDS
350 samples clustered distinctly from normal bone marrow, with *TP53*-mutated samples showing unique clustering.
351 MDS-MAPS values aligned with IPSS-M scores in most cases; however, approximately half of IPSS-M lower
352 risk patients were characterized by higher risk MDS-MAPS values, indicating a potential for this metric to identify
353 patients whose disease course may not be accurately assessed using current models. Because we lack the cohort
354 size for a predictive model of overall survival or AML progression, we conducted a preliminary analysis of sixteen
355 patients who received DMTs, including 8 patients who experienced disease progression. Our results suggest that
356 microarchitectural parameters, in addition to the clinical and hematologic parameters of the current models, could
357 enable refined prognostication. Notably, patch-level MDS-MAPS analyses revealed greater intra-tissue

358 heterogeneity in low-grade MDS compared to high-grade or NBM samples, indicating that early MDS may
359 exhibit more variable spatial changes, which could be overlooked in studies using aspirated marrow.

360 We also evaluated serial bone marrow samples collected from patients treated using standard-of-care
361 pharmacologic agents. For patients who achieved remission, at that time, we observed architectural features
362 reminiscent of an NBM-like state, including reduced ALIP density, re-localization of HSPCs near vasculature,
363 and normalized megakaryocyte morphology. However, in patients with disease recurrence, these improvements
364 reverted to baseline, reinforcing the connection between microarchitectural changes and disease state.

365 Here, we demonstrate the potential of high-resolution spatial biology to characterize perturbations of the
366 microarchitecture of hematopoiesis in MDS patients. Using an AI-driven approach to quantify microarchitectural
367 alterations in patient samples, we identify genotype- and disease severity-specific patterns that are not captured
368 by traditional histopathology. While our treatment-naïve cohort is relatively small, we believe this limitation is
369 balanced by the interrogation of cell type frequencies, cytomorphologic features and cell-cell and cell-tissue
370 structure relationships across millions of spatially-resolved single cells. Furthermore, by profiling serial samples,
371 we control for biologically and clinical important variables such as sex, age, complex mutational profiles, and
372 inherited genetic background in several patients. Our findings have important implications for clinical practice
373 and lay the foundation for spatial analysis to be integrated into diagnostic workflows to enhance prognostication
374 and treatment monitoring for MDS patients. Although further validation in clinical trials is needed, this approach
375 holds promise for significantly improving the standard of care in MDS diagnosis and management.

376

377

378

379

380

381

METHODS

Patients

Individuals who underwent a posterior iliac crest bone marrow biopsy, to evaluate for cytopenia of unknown etiology, were considered for inclusion in the study. Archival decalcified, bouin-fixed, and paraffin-embedded posterior iliac crest trephine bone marrow (BM) biopsy tissues were originally collected for routine diagnostic evaluation at Weill Cornell Medical College/NewYork-Presbyterian Hospital (WCM/NYP). Although two classification schema currently exist for MDS (World Health Organization 5th Edition [WHO] and International Consensus Classification [ICC]), WHO criteria were selected for streamlining and unifying case labeling. The cohort included patients diagnosed with MDS or CHIP/CCUS (n=48 unique patients), and serial samples (n=29) were collected for 14 MDS patients (n=14, range 2-7 samples/patient). Normal bone marrow (NBM) controls from a recently published cohort were also included (n=21).[11] All samples from CHIP/CCUS and MDS patients had undergone a comprehensive diagnostic hematopathology evaluation, involving conventional histomorphologic assessment, flow cytometry (MFC) and immunohistochemistry-based immunophenotyping, cytogenetic analysis, and targeted next-generation sequencing; all available ancillary data were collected. Complete blood count (CBC) with differential were also collected for these patients.

Hematoxylin and eosin (H&E)-stained preparations from all NBM, CHIP/CCUS, and MDS samples were re-reviewed (SSP) to ensure the material was of adequate quantity and quality to be utilized for subsequent testing. Following Institutional Review Board (IRB) approval, and in accordance with the Declaration of Helsinki, archival trephine biopsy samples were further evaluated using a pipeline for whole slide multiplex immunofluorescence tissue staining, whole slide imaging, and artificial intelligence (AI)-based image analysis (**Figure 1a, Supplementary Data Figure 1a**). Whole slide images (WSIs) of each H&E-stained preparation were also captured using the Vectra Polaris Automated Quantitative Pathology Imaging System (Akoya Biosciences, Marlborough, MA). Bone marrow samples from 7 additional MDS patients with *TP53* DNA binding domain

missense mutations, along with 5 additional NBMs, were included in a tissue microarray (TMA) [see below] for select analyses.

All MDS patients were treated as per standard-of-care, including non-disease-modifying interventions (e.g., therapeutic red cell and/or platelet transfusion, erythropoiesis stimulating agents), disease-modifying pharmacologic therapies (DMTs, n=25; e.g., hypomethylating agents (HMAs) with or without venetoclax), and allogeneic hematopoietic stem cell transplantation (HSCT, n=3) in a small subset of patients **(Supplementary Data Table 1).** Per 2023 MDS International Working Group (IWG) response criteria, among 25 patients who received DMTs during their disease course, 9 achieved at least limited count recovery (CRL). Among 18 patients with longitudinal bone marrow evaluations at our institution, 9 experienced progressive increases in marrow blast percentages while receiving DMTs (**Supplementary Data Table 3**). Additional details are provided in **Supplementary Materials**.

Multiparameter Flow Cytometry (MFC)

Multiparameter flow cytometry (10-color) was performed using the EuroFlow panel design.[47] MFC results were analyzed with BD FACSDiva software (BD Biosciences, San Jose, CA). Gating was performed using forward scatter parameters (FSC-A/FSC-H) to identify singlets, CD45/Viability Dye to identify viable cells, and CD45 by side scatter (SSC) gating to identify blast, lymphocyte, monocyte, and granulocyte subpopulations. Orthogonal flow cytometry data were available for all samples included in the study (n=99), with consistent assessment of percentages of lymphocytes, granulocytes, and monocytes. A minimum of 200,000 events were collected for all samples. All flow cytometry data were re-reviewed (SSP) and percentages for the following cell populations were determined based on available markers on a per-case basis: mature lymphocytes, granulocytes, monocytes, CD34+/CD117+ myeloblasts, CD117+/CD15+ promyelocytes, total CD15+ cells, total CD71+ cells, CD117+/CD71+ proerythroblasts, CD45+(low)/CD38+/CD117-negative putative B-cell precursors

438 (hematogones), CD38+(high) plasma cells, and mast cells. Details for all samples are provided in **Supplementary**
439 **Data Table 2**.

440 ***Cytogenetic and Fluorescence In-Situ Hybridization (FISH) Studies***

441 Conventional cytogenetic analysis was performed on G-banded metaphase cells prepared from bone
442 marrow aspirate or lymph node cultures using standard techniques. Twenty metaphases were analyzed and the
443 results were reported using the International System for Human Cytogenetic Nomenclature. Fluorescence in situ
444 hybridization (FISH) was performed where indicated and as feasible using multiplex probes LSI D5S23/D5S721
445 (5p15.2)/EGR1 (5q31) and CEP 7/D7S486 (7q31), and single probes CEP 8 (8p11.1-q11.1), LSI D20S108
446 (20q12) (Vysis/Abbott Molecular Inc., Des Plaines, IL), and LSI TP53 (17p13.1, SO) (Vysis/Abbott Molecular
447 Inc., Des Plaines, IL) to rule out monosomy 5/deletion 5q31, monosomy 7/deletion 7q31, trisomy 8, deletion
448 20q12, and *TP53* deletion, respectively. Two hundred interphase nuclei were screened for each
449 probe. Cytogenetic data for available samples are included in **Supplementary Data Table 1**.

450

451 ***Next-Generation Sequencing***

452 A custom 45 gene NGS panel [Thunderstorm system, RainDance Technologies, Billerica, MA, USA]
453 interrogating single nucleotide variants (SNVs) and insertion/deletions (InDels) was used to profile the majority
454 of the bone marrow samples (n=47). Sequencing was performed using Illumina MiSeq (v3 chemistry) and
455 samples were run in duplicate. The analytical sensitivity for this assay was approximately 2% for SNV and 1%
456 for InDels. In addition, TruSight Oncology 500 (TSO500) assay, a 523-gene hybridization capture–based panel
457 (Illumina Inc., San Diego, CA, USA) was used to profile SNVs and InDels in the remaining bone marrow samples
458 based on availability of retained cell pellets (n=32). DNA was extracted from cell pellets, library was prepared
459 according to manufacturer's specifications, and sequencing was performed on the Illumina NovaSeq6000.
460 Bioinformatic analysis was performed using Local App version 2.2 (Illumina). The analytical sensitivity of

461 TSO500 assay for SNVs and indels was approximately 3% variant allele frequency. Both sequencing assays were
462 approved by New York State for clinical use. Details for all samples are provided in **Supplementary Data Table**
463 **4**.

464 ***Tissue Microarray Construction***

465 Formalin-fixed paraffin-embedded human bone marrow clot section material was used to create a tissue
466 microarray (TMA). One-millimeter cores were extracted from original tissue blocks and deposited in duplicate
467 or triplicate into a recipient paraffin block using Tissue-Tek® Quick-Ray™ 1mm (Ref: 8016). The TMA included
468 samples from patients with *TP53*-mutated MDS-LB or MDS-IB (WCM14, WCM15, WCM78, WCM79,
469 WCM80, WCM81, WCM82), including two patients also included in the main trephine biopsy cohort (WCM14,
470 WCM15). All *TP53* mutations were located in the DNA binding domain, leading to mutant p53 protein
471 accumulation detectable by immunohistochemistry. Five normal bone marrow samples were included as controls
472 (WCM83, WCM84, WCM85, WCM86, WCM87). Details of staining and imaging of the TMA are provided in
473 the "Multiplex Immunofluroescence Tissue Staining" section below. Representative single channel and multiplex
474 images from human tonsil, normal bone marrow controls, and *TP53*-mutated MDS-LB and MDS-IB cases are
475 provided in **Supplementary Materials**.

476

477 ***Multiplex Immunofluorescence Tissue Staining***

478 Multiplex immunofluorescence (MxIF) staining was performed using the Opal system (Akoya
479 Biosciences, Marlborough, MA) as previously described.[11,48,49] Additional details are provided in
480 **Supplementary Materials**.

481 ***Artificial Intelligence (AI)-based Digital Image Analysis***

482 We leveraged established computer vision techniques and open-source software to extract individual cell
483 and structural component locations, morphology, phenotypes, and spatial patterns from MxIF WSIs. The goal
484 was to perform segmentation in which the boundaries of individual cells are defined and assigned coordinates,
485 create phenotypes according to cell morphology and membrane marker expression to automate identification of
486 bone marrow components (vasculature, bone trabeculae, and fat), and to detect communities of cells such as
487 erythroid islands, and Atypical Localization of Immature Precursors (ALIP) clusters. Additional details related to
488 cell segmentation, phenotyping, and cytomorphologic analyses are provided in **Supplementary Materials**.

489 *Permutation Testing*

490 Permutation testing was used to quantify spatial enrichment of cell types in relation to specific structural
491 components (endothelium, and bone trabeculae). This involved quantifying the distribution of cell locations to
492 structural components as compared between observed and randomly reassigned cell x-y coordinates. Permutations
493 were shuffled 1,000 times for robustness. All hematopoietic cell locations were used as coordinates for randomly
494 generated cell identities, and cell phenotypes were sampled without replacement. P-values were determined as
495 the frequency of permutations where the randomly shuffled cell assignments showed equal or greater proximity
496 to the structural component. Therefore, the permutation testing P-value represents the probability against the null
497 hypothesis that the given cell type population tested was not at all spatially enriched within a predefined distance
498 (e.g., 15µm or 30µm) from the structural component. Given the distribution of vascular elements within the
499 cellular milieu of the bone marrow, we used a radius of 15µm to assess spatial proximity of hematopoietic cells
500 to vascular elements. Conversely, to assess for hematopoietic cell enrichment near trabeculae we employed a
501 radius of 30µm because trabeculae are larger structures that more dramatically define the tissue structure. Python
502 libraries Scimap and Scipy.spatial were used for permutation testing and distance computation. Illustrative visual
503 examples are provided in **Supplementary Materials**.

504 *Erythroid Cluster Density and Rolling Signal-based Ripley's K Statistic Analyses*

We applied two spatial pattern analysis techniques to quantify the degree of clustering of Erythroid Normoblast within a WSI. In both cases, Erythroid Normoblast locations were modeled as point patterns of x-y coordinates. Ripley's K function is a standard method for determining clustering of a point pattern and involves quantifying the occurrences of points within proximity to each other in a pattern as compared with a random theoretical distribution of the same number of points. Since in a WSI, thousands of Erythroid Normoblast points are distributed across a heterogeneous space, we used a method designed for such cases. Rolling Signal-based Ripley's K computes the K statistic within distinct regions of the tissue and averages together values computed across sliding windows to quantify the K statistic in the whole tissue.[6] This K statistic was tested at multiple distance radii to observe how Erythroid Normoblast clustering distributions changed at sequential distance intervals, and square regions of 256x256µm were used as the window size for the rolling signal local computation. We designed the second method since the generally observed behavior of Erythroid Normoblasts is to form island-like clusters across the bone marrow. We used Hierarchical DBSCAN clustering, a density-based unsupervised clustering method, to identify distinct clusters of Erythroid Normoblast coordinates throughout the tissue. Spatial statistics were calculated on the individual cluster level, such as the density of the number of points within the area covered by the cluster boundary and the clustering coefficient as computed from the nearest neighbor distances of the cluster graph. Python libraries Scikit-Learn, NetworkX, and hdbscan were used. Examples are provided in **Supplementary Materials**.

Atypical Localization of Immature Precursors Analysis

To quantify the feature of atypical localization of immature precursors (ALIPs), generally defined as clusters of 2-3 immature myeloid progenitors located in central intertrabecular regions, we constructed a nearest neighbor graph of all Myeloblasts and Promyelocytes and set a connection distance threshold of 12 microns to distinguish clusters of immature myeloid progenitors (myeloblasts/promyelocytes). Clusters that were located greater than 150 microns from bone trabeculae and 40 microns from endothelium were classified as ALIP clusters. Examples are provided in **Supplementary Materials**.

MDS Microarchitectural Perturbation Score (MDS-MAPS)

Because we observed spatial heterogeneity in the manifestation of MDS features, we split each WSI into smaller "patches" (256x256μm) to compute features at the patch level and maintain information inherent to the spatial biology. To quantify in a single metric the presentation of characteristic MDS features, we created the MDS Microarchitectural Perturbation Score (MDS-MAPS), which combined locally computed cell intrinsic, morphological, and spatially determined features in an additive model. Model weights were derived by sample-level stratification of cases by disease severity, and expert adjustment of pathological criteria. For comparing mean MAPS values between WSI samples, we filtered out any region with less than 100 cells or a proportion of Non-Hematopoietic Elements greater than 95 percent. Sample level entropy was computed using normalized continuous entropy of the two-dimensional patch level MAPS value heatmap and represents the disorder or randomness of each WSI sample's score values. Patch size of 256x 256μm was determined as the most viable patch size with the highest spatial resolution after computing basic statistics for different increments of patch sizes. Patch-level MAPS is the sum of patch-level feature observations weighted by these feature importance scores and represents an individual score for each patch in a tissue sample. Illustrative case examples with accompanying single channel image data are provided in **Supplementary Materials**.

Statistical Analyses

Statistical analyses were performed in Python (v3.11), using the scipy (v1.11.4) and statsmodels (0.14.5) packages. The Mann-Whitney U test was used for pairwise group comparisons, and Spearman's correlation coefficient was used for correlation testing, if not otherwise specified. Multiple comparisons correction (Benjamini-Hochberg procedure) was applied to high-dimensional analyses including differential gene expression testing. Statistical significance was defined as $p < .05$ unless otherwise stated. Stouffer's method was used for combining p-values between groups.

552 **REFERENCES**

553 1. Cazzola M. Myelodysplastic Syndromes. *N Engl J Med*. 2020;383(14):1358-1374.
554 doi:10.1056/NEJMra1904794

555 2. Hasserjian RP, Germing U, Malcovati L. Diagnosis and classification of myelodysplastic syndromes.
556 *Blood*. 2023;142(26):2247-2257. doi:10.1182/blood.2023020078

557 3. Yuen LD, Hasserjian RP. Morphologic Characteristics of Myelodysplastic Syndromes. *Clin Lab Med*.
558 2023;43(4):577-596. doi:10.1016/j.cll.2023.06.003

559 4. Barone P, Patel S. Myelodysplastic syndrome: Approach to diagnosis in the era of personalized medicine.
560 *Semin Diagn Pathol*. 2023;40(3):172-181. doi:10.1053/j.semdp.2023.04.008

561 5. Greenberg PL, Tuechler H, Schanz J, et al. Revised International Prognostic Scoring System for
562 Myelodysplastic Syndromes. *Blood*. 2012;120(12):2454-2465. doi:10.1182/blood-2012-03-420489

563 6. Bernard E, Tuechler H, Greenberg PL, et al. Molecular International Prognostic Scoring System for
564 Myelodysplastic Syndromes. *NEJM Evid*. 2022;1(7):EVIDoa2200008. doi:10.1056/EVIDoa2200008

565 7. Aster JC. What is in a Name? Consequences of the Classification Schism in Hematopathology. *J Clin*
566 *Oncol*. Published online 10 March 2023. doi:10.1200/JCO.22.02680

567 8. Pronk E, Raaijmakers MHGP. The mesenchymal niche in MDS. *Blood*. 2019;133(10):1031-1038.
568 doi:10.1182/blood-2018-10-844639

569 9. Mina A, Pavletic S, Aplan PD. The evolution of preclinical models for myelodysplastic neoplasms.
570 *Leukemia*. 2024;38(4):683-691. doi:10.1038/s41375-024-02181-2

571 10. Munteanu R, Gulei D, Moldovan CS, et al. Humanized mouse models in MDS. *Cell Death Dis*.
572 2025;16(1):531. doi:10.1038/s41419-025-07861-0

573 11. Sarachakov A, Varlamova A, Svelolkin V, et al. Spatial Mapping of Human Hematopoiesis at Single Cell
574 Resolution Reveals Aging-Associated Topographic Remodeling. *Blood*. Published online 29 September
575 2023:blood.2023021280. doi:10.1182/blood.2023021280

576 12. Will B, Zhou L, Vogler TO, et al. Stem and progenitor cells in myelodysplastic syndromes show aberrant
577 stage-specific expansion and harbor genetic and epigenetic alterations. *Blood*. 2012;120(10):2076-2086.
578 doi:10.1182/blood-2011-12-399683

579 13. Fernandez-Pol S, Ma L, Ohgami RS, Arber DA. Immunohistochemistry for p53 is a useful tool to identify
580 cases of acute myeloid leukemia with myelodysplasia-related changes that are TP53 mutated, have complex
581 karyotype, and have poor prognosis. *Mod Pathol Off J U S Can Acad Pathol Inc*. 2017;30(3):382-392.
582 doi:10.1038/modpathol.2016.206

583 14. Tashakori M, Kadia T, Loghavi S, et al. TP53 copy number and protein expression inform mutation status
584 across risk categories in acute myeloid leukemia. *Blood*. 2022;140(1):58-72.
585 doi:10.1182/blood.2021013983

586 15. McGraw KL, Nguyen J, Komrokji RS, et al. Immunohistochemical pattern of p53 is a measure of TP53
587 mutation burden and adverse clinical outcome in myelodysplastic syndromes and secondary acute myeloid
588 leukemia. *Haematologica*. 2016;101(8):e320-323. doi:10.3324/haematol.2016.143214

589 16. Avecilla ST, Hattori K, Heissig B, et al. Chemokine-mediated interaction of hematopoietic progenitors with
590 the bone marrow vascular niche is required for thrombopoiesis. *Nat Med*. 2004;10(1):64-71.
591 doi:10.1038/nm973

592 17. Möhle R, Bautz F, Rafii S, Moore MAS, Brugger W, Kanz L. The Chemokine Receptor CXCR-4 Is
593 Expressed on CD34+Hematopoietic Progenitors and Leukemic Cells and Mediates Transendothelial
594 Migration Induced by Stromal Cell-Derived Factor-1. *Blood*. 1998;91(12):4523-4530.
595 doi:10.1182/blood.V91.12.4523

596 18. Jann JC, Schmitt N, Streuer A, et al. Instructive interaction between myelodysplastic hematopoiesis and the
597 bone marrow microenvironment at the single-cell level. *Blood Neoplasia*. 2024;1(3):100021.
598 doi:10.1016/j.bneo.2024.100021

599 19. Matsuda M, Morita Y, Hanamoto H, Tatsumi Y, Maeda Y, Kanamaru A. CD34+ progenitors from MDS
600 patients are unresponsive to SDF-1, despite high levels of SDF-1 in bone marrow plasma. *Leukemia*.
601 2004;18(5):1038-1040. doi:10.1038/sj.leu.2403301

602 20. Im H, Rao V, Sridhar K, et al. Distinct transcriptomic and exomic abnormalities within myelodysplastic
603 syndrome marrow cells. *Leuk Lymphoma*. 2018;59(12):2952-2962. doi:10.1080/10428194.2018.1452210

604 21. Ganan-Gomez I, Yang H, Ma F, et al. Stem cell architecture drives myelodysplastic syndrome progression
605 and predicts response to venetoclax-based therapy. *Nat Med*. 2022;28(3):557-567. doi:10.1038/s41591-022-
606 01696-4

607 22. Behbehani GK, Finck R, Samusik N, et al. Profiling myelodysplastic syndromes by mass cytometry
608 demonstrates abnormal progenitor cell phenotype and differentiation. *Cytometry B Clin Cytom*.
609 2020;98(2):131-145. doi:10.1002/cyto.b.21860

610 23. Buesche G, Teoman H, Giagounidis A, et al. Impaired formation of erythroblastic islands is associated with
611 erythroid failure and poor prognosis in a significant proportion of patients with myelodysplastic syndromes.
612 *Haematologica*. 2016;101(5):5. doi:10.3324/haematol.2015.129015

613 24. Kayano H. Histopathology in the diagnosis of high-risk myelodysplastic syndromes. *J Clin Exp Hematop*
614 *JCEH*. 2018;58(2):51-60. doi:10.3960/jslrt.18009

615 25. Valent P, Büsche G, Theurl I, et al. Normal and pathological erythropoiesis in adults: from gene regulation
616 to targeted treatment concepts. *Haematologica*. 2018;103(10):1593-1603.
617 doi:10.3324/haematol.2018.192518

618 26. Zhang J, Niu C, Ye L, et al. Identification of the haematopoietic stem cell niche and control of the niche
619 size. *Nature*. 2003;425(6960):836-841. doi:10.1038/nature02041

620 27. De Wolf-Peeters C, Stessens R, Desmet V, Tricot G, Verwilghen RL. The histological characterization of
621 ALIP in the myelodysplastic syndromes. *Pathol Res Pract*. 1986;181(4):402-407. doi:10.1016/S0344-
622 0338(86)80075-9

623 28. Oriani A, Annaloro C, Soligo D, Pozzoli E, Cortelezzi A, Lambertenghi Deliliers G. Bone marrow
624 histology and CD34 immunostaining in the prognostic evaluation of primary myelodysplastic syndromes.
625 *Br J Haematol*. 1996;92(2):360-364. doi:10.1046/j.1365-2141.1996.d01-1484.x

626 29. Della Porta MG, Malcovati L, Boveri E, et al. Clinical Relevance of Bone Marrow Fibrosis and CD34-
627 Positive Cell Clusters in Primary Myelodysplastic Syndromes. *J Clin Oncol*. 2009;27(5):754-762.
628 doi:10.1200/JCO.2008.18.2246

629 30. Wu Q, Zhang J, Lucas D. Anatomy of Hematopoiesis and Local Microenvironments in the Bone Marrow.
630 Where to? *Front Immunol*. 2021;12:768439. doi:10.3389/fimmu.2021.768439

631 31. Wu Q, Zhang J, Kumar S, et al. Resilient anatomy and local plasticity of naive and stress haematopoiesis.
632 *Nature*. 2024;627(8005):839-846. doi:10.1038/s41586-024-07186-6

633 32. Zhang J, Wu Q, Johnson CB, et al. In situ mapping identifies distinct vascular niches for myelopoiesis.
634 *Nature*. 2021;590(7846):457-462. doi:10.1038/s41586-021-03201-2

635 33. Puhm F, Laroche A, Boilard E. Diversity of Megakaryocytes. *Arterioscler Thromb Vasc Biol*.
636 2023;43(11):2088-2098. doi:10.1161/ATVBAHA.123.318782

637 34. Di Giandomenico S, Kermani P, Mollé N, et al. Megakaryocyte TGFβ1 partitions erythropoiesis into
638 immature progenitor/stem cells and maturing precursors. *Blood*. 2020;136(9):1044-1054.
639 doi:10.1182/blood.2019003276

640 35. Acar M, Kocherlakota KS, Murphy MM, et al. Deep imaging of bone marrow shows non-dividing stem
641 cells are mainly perisinusoidal. *Nature*. 2015;526(7571):126-130. doi:10.1038/nature15250

642 36. Heissig B, Hattori K, Dias S, et al. Recruitment of stem and progenitor cells from the bone marrow niche
643 requires MMP-9 mediated release of kit-ligand. *Cell*. 2002;109(5):625-637. doi:10.1016/s0092-
644 8674(02)00754-7

645 37. Rafii S, Shapiro F, Pettengell R, et al. Human Bone Marrow Microvascular Endothelial Cells Support
646 Long-Term Proliferation and Differentiation of Myeloid and Megakaryocytic Progenitors. *Blood*.
647 1995;86(9):3353-3363. doi:10.1182/blood.V86.9.3353.bloodjournal8693353

648 38. Gomez-Salinero JM, Redmond D, Rafii S. Microenvironmental determinants of endothelial cell
649 heterogeneity. *Nat Rev Mol Cell Biol*. 2025;26(6):476-495. doi:10.1038/s41580-024-00825-w

650 39. Pinho S, Frenette PS. Haematopoietic stem cell activity and interactions with the niche. *Nat Rev Mol Cell*
651 *Biol*. 2019;20(5):303-320. doi:10.1038/s41580-019-0103-9

652 40. Butler JM, Nolan DJ, Vertes EL, et al. Endothelial cells are essential for the self-renewal and repopulation
653 of Notch-dependent hematopoietic stem cells. *Cell Stem Cell*. 2010;6(3):251-264.
654 doi:10.1016/j.stem.2010.02.001

655 41. Hooper AT, Butler JM, Nolan DJ, et al. Engraftment and reconstitution of hematopoiesis is dependent on
656 VEGFR2-mediated regeneration of sinusoidal endothelial cells. *Cell Stem Cell*. 2009;4(3):263-274.
657 doi:10.1016/j.stem.2009.01.006

42. Kobayashi H, Butler JM, O'Donnell R, et al. Angiocrine factors from Akt-activated endothelial cells balance self-renewal and differentiation of haematopoietic stem cells. *Nat Cell Biol*. 2010;12(11):1046-1056. doi:10.1038/ncb2108

43. Li Q, Wang M, Zeng L, et al. Deletion of Wild-type p53 Facilitates Bone Metastatic Function by Blocking the AIP4 Mediated Ligand-Induced Degradation of CXCR4. *Front Pharmacol*. 2021;12:792293. doi:10.3389/fphar.2021.792293

44. Moura PL, Mortera-Blanco T, Hofman IJ, et al. Erythroid Differentiation Enhances RNA Mis-Splicing in SF3B1-Mutant Myelodysplastic Syndromes with Ring Sideroblasts. *Cancer Res*. 2024;84(2):211-225. doi:10.1158/0008-5472.CAN-23-3038

45. De La Garza A, Cameron RC, Gupta V, Fraint E, Nik S, Bowman TV. The splicing factor Sf3b1 regulates erythroid maturation and proliferation via TGFβ signaling in zebrafish. *Blood Adv*. 2019;3(14):2093-2104. doi:10.1182/bloodadvances.2018027714

46. Lieu YK, Liu Z, Ali AM, et al. SF3B1 mutant-induced missplicing of MAP3K7 causes anemia in myelodysplastic syndromes. *Proc Natl Acad Sci U S A*. 2022;119(1):e2111703119. doi:10.1073/pnas.2111703119

47. van Dongen JJM, Lhermitte L, Böttcher S, et al. EuroFlow antibody panels for standardized n-dimensional flow cytometric immunophenotyping of normal, reactive and malignant leukocytes. *Leukemia*. 2012;26(9):9. doi:10.1038/leu.2012.120

48. Berry S, Giraldo NA, Green BF, et al. Analysis of multispectral imaging with the AstroPath platform informs efficacy of PD-1 blockade. *Science*. 2021;372(6547):eaba2609. doi:10.1126/science.aba2609

49. Patel SS, Weirather JL, Lipschitz M, et al. The microenvironmental niche in classic Hodgkin lymphoma is enriched for CTLA-4-positive T cells that are PD-1-negative. *Blood*. 2019;134(23):2059-2069. doi:10.1182/blood.2019002206

DATA AVAILABILITY

All data and code will be deposited online (https://github.com/BoneMarrowMxIFImaging/MDS.Manuscript) following formal manuscript review.

AUTHOR CONTRIBUTIONS

Conceptualization: S.P. *Methodology*: R.N., D.R., S.P. *Formal analysis*: R.N., D.R. *Investigation*: R.N., A.K., J.C., A.R., I.V., C.U., J.J., F.S., J.P., C.M., L.Z., D.S., G.R., P.D., J.K., J.F., M.G., N.L., A.C., M.O., P.S., J.G.,

G.I., S.R., D.R., S.P., *Visualization*: R.N. *Resources*: N.L., G.I., S.R., S.P. *Writing*: R.N., S.P. *Supervision*: D.R., S.P. *Funding acquisition*: S.R., S.P.

FUNDING

S.R is supported by NIH funding (R35HL150809). The other authors have no relevant funding to disclose.

COMPETING INTERESTS

The authors declare no competing interests relevant to this study.

ACKNOWLEDGEMENTS

This work was supported by the Department of Pathology and Laboratory Medicine, Weill Cornell Medical College (start-up funding to S.S.P.). Tissue staining and imaging was performed in the Multiparametric In Situ Imaging (MISI) Laboratory of the Department of Pathology and Laboratory Medicine, Weill Cornell Medical College.